



HIDDEN ACTIVE GALACTIC NUCLEI IN EARLY-TYPE GALAXIES

ALESSANDRO PAGGI¹, GIUSEPPINA FABBIANO¹, FRANCESCA CIVANO^{1,2}, SILVIA PELLEGRINI³, MARTIN ELVIS¹, AND DONG-WOO KIM¹¹Harvard-Smithsonian Center for Astrophysics, 60 Garden St, Cambridge, MA 02138, USA; apaggi@cfa.harvard.edu²Department of Physics and Yale Center for Astronomy and Astrophysics, Yale University, P.O. Box 208121, New Haven, CT 06520-8121, USA³Department of Astronomy, University of Bologna, via Ranzani 1, I-40127 Bologna, Italy

Received 2015 July 11; accepted 2016 April 7; published 2016 May 27

ABSTRACT

We present a stacking analysis of the complete sample of early-type galaxies (ETGs) in the *Chandra* COSMOS (C-COSMOS) survey, to explore the nature of the X-ray luminosity in the redshift and stellar luminosity ranges $0 < z < 1.5$ and $10^9 < L_K/L_\odot < 10^{13}$. Using established scaling relations, we subtract the contribution of X-ray binary populations to estimate the combined emission of hot ISM and active galactic nuclei (AGNs). To discriminate between the relative importance of these two components, we (1) compare our results with the relation observed in the local universe $L_{X,\text{gas}} \propto L_K^{4.5}$ for hot gaseous halos emission in ETGs, and (2) evaluate the spectral signature of each stacked bin. We find two regimes where the non-stellar X-ray emission is hard, consistent with AGN emission. First, there is evidence of hard, absorbed X-ray emission in stacked bins including relatively high z (~ 1.2) ETGs with average high X-ray luminosity ($L_{X\text{-LMXB}} \gtrsim 6 \times 10^{42} \text{ erg s}^{-1}$). These luminosities are consistent with the presence of highly absorbed “hidden” AGNs in these ETGs, which are not visible in their optical–IR spectra and spectral energy distributions. Second, confirming the early indication from our C-COSMOS study of X-ray detected ETGs, we find significantly enhanced X-ray luminosity in lower stellar mass ETGs ($L_K \lesssim 10^{11} L_\odot$), relative to the local $L_{X,\text{gas}} \propto L_K^{4.5}$ relation. The stacked spectra of these ETGs also suggest X-ray emission harder than expected from gaseous hot halos. This emission is consistent with inefficient accretion $10^{-5} - 10^{-4} \dot{M}_{\text{Edd}}$ onto $M_{\text{BH}} \sim 10^6 - 10^8 M_\odot$.

Key words: galaxies: elliptical and lenticular, cD – surveys – X-rays: galaxies

1. INTRODUCTION

Diffuse X-ray emission from normal early-type galaxies (ETGs) was first detected in the Virgo cluster with the *Einstein* X-ray Observatory (Forman et al. 1979). Although in a few cases (e.g., M86) the displacement of the X-ray emission from the stellar body of the galaxy pointed to hot gaseous halos, the \sim arcminute resolution of the *Einstein* IPC data could not disentangle observationally hot halos from the populations of low-mass X-ray binaries (LMXBs), which was likely to dominate the X-ray emission in a large number of the observed ETGs (Trinchieri & Fabbiano 1985). Nonetheless, several authors discussed how the X-ray emission and the inferred hot gas contribution could be used to constrain both the binding mass of the galaxies and the physical evolution of the hot halos, including feedback from SNIa and active galactic nuclei (AGNs), and interaction with intracluster and group media (see e.g., Canizares et al. 1987; Fabbiano 1989; Ciotti et al. 1991; David et al. 1991; White & Sarazin 1991; Mathews & Brighenti 2003; Ciotti & Ostriker 2007).

Thanks to the high spatial resolution of *Chandra* and the imaging/spectral capabilities of the ACIS detector (Garmire et al. 2003), it has become possible to directly detect and characterize the different contributions to the X-ray emission of ETGs in the near universe. With *Chandra*, LMXB populations—both associated with globular clusters (GC) and in the stellar field of the ETG—have been studied to distances of several tens of megaparsecs (e.g., Sarazin et al. 2000; Kundu et al. 2002; see review by Fabbiano 2006). The integrated LMXB luminosity correlates well with the integrated ETG stellar luminosity (e.g., Kim & Fabbiano 2004; Gilfanov 2004). The scatter in this relation is a factor of 2–3, and it depends on both the GC content (Kim & Fabbiano 2004) and the age of the stellar population (Kim et al. 2009; Kim & Fabbiano 2010;

Borson et al. 2011; Lehmer et al. 2014). These detailed high resolution studies allowed Borson et al. (2011, BKF11) to accurately estimate the gaseous contribution to the X-ray luminosity $L_{X,\text{gas}}$ of a sample of 30 ETGs within 32 Mpc. After subtracting the LMXB, stellar, and nuclear contributions to the X-ray luminosity, BKF11 found steep scaling relations between $L_{X,\text{gas}}$ and both the stellar L_K luminosity and the hot gas temperature T . Subsequent work by Kim & Fabbiano (2013, KF13; 2015, KF15) suggests that for $L_{X,\text{gas}} > 10^{40} \text{ erg s}^{-1}$ the hot gas around ETGs is virialized, giving a new way to measure the total mass of these galaxies.

Beyond the local universe, *Chandra* Deep Field studies (both detections and stacking of almost 1000 ETGs) found that the mean L_X of $L_B = 10^{10} L_\odot$ ETGs remains equal or slightly increases over $z = 0 - 0.7$ (Lehmer et al. 2007; Tzanavaris & Georgantopoulos 2008) and that the ratio of the soft X-ray luminosity to the B-band luminosity evolves mildly as $L_{(0.5-2\text{keV})}/L_B \propto (1+z)^{1.1 \pm 0.7}$ since $z \approx 1.2$ (Danielson et al. 2012), suggesting some heating mechanism preventing the hot gas from cooling, consistent with mechanical heating from radio AGNs. The evolution of the X-ray binary contribution to the X-ray emission (both of LMXBs and high mass binaries) across cosmic time, modeled by Fragos et al. (2013a), led Fragos et al. (2013b) to conclude that energy feedback from X-ray binaries is also important in the early universe.

The COSMOS survey, covering ~ 2 square degrees of sky with multi-wavelength coverage, which includes *Chandra* X-ray coverage (Scoville et al. 2007; Elvis et al. 2009), has increased the available sample of ETGs to over 6600 galaxies Civano et al. (2014, C14). This survey provides a good z coverage out to $z \sim 2.5$ (and a few galaxies are detected out to $z \sim 5$). C14 studied the sample of 69 X-ray detected ETGs in

the *Chandra* COSMOS survey (C-COSMOS, Elvis et al. 2009), covering a redshift range $0 < z < 1.5$, to explore redshift dependencies in the BKF11, KF13 scaling relations. In particular, C14 focused on the relation between $L_{X,\text{gas}}$ and the K-band stellar luminosity (L_K) of ETGs which is a good proxy of stellar mass for old stellar systems. The latter has been evaluated in the local universe by BKF11 as $L_{X,\text{gas}} \propto L_K^{2.6 \pm 0.4}$ for sources with $L_{X,\text{gas}} \leq 2 \times 10^{41} \text{ erg s}^{-1}$, while including sources with $L_{X,\text{gas}}$ up to $9 \times 10^{42} \text{ erg s}^{-1}$ KF13 found a steeper $L_{X,\text{gas}} \propto L_K^{4.5 \pm 0.8}$ relation. C14 found that this latter relation also holds for X-ray detected ETGs with $L_{X,\text{gas}} \leq 10^{42} \text{ erg s}^{-1}$, suggesting that the hot gas in these more distant galaxies may be virialized as well. However, more distant ($z > 0.9$) and younger stellar age galaxies generally fall outside the relation observed in the local sample, and are X-ray over-luminous with respect to their L_K . For these sources C14 suggested that the higher X-ray luminosity may be due to the presence of hidden AGNs (as suggested by observed hardness ratios, HRs), merging phenomena, which are expected to increase the halo X-ray luminosity, or nuclear accretion (which could also induce AGN activity during the merging phase, Cox et al. 2006).

In this work we perform a stacking analysis of the C-COSMOS ETG data in order to investigate the nature of fainter, X-ray undetected ETGs. We compare their properties with those of the sample of local ETGs investigated by BKF11 and KF13, and with the sample of ETGs detected in the C-COSMOS survey studied by C14. This stacking study also allow us to further explore redshift dependencies. Our aim is to explore the properties of the non-stellar X-ray emission, i.e., the X-ray emission resulting from the subtraction of the expected X-ray binary contribution (taking into account the cosmic evolution of the X-ray binary population Fragos et al. 2013b). The resulting emission will probe both hot X-ray halos and the possible emission of active nuclei in these galaxies. In particular, the large number of low-stellar-mass ETGs in the sample will provide a unique probe of the existence of relatively low-mass massive black holes in their nuclei. These black holes should produce low-luminosity nuclear X-ray sources, if they are fueled by the ETG stellar outgassing (Volonteri et al. 2011).

The paper is organized as follows: Section 2 describes the sample selection and the datasets used in this work, Section 3.3 is dedicated to the description of the adopted stacking procedure, in Section 4 we discuss our results, and Section 5 is dedicated to our conclusions. In the following, we adopt the standard flat cosmology with $\Omega_\Lambda = 0.73$ and $H_0 = 70 \text{ km s}^{-1} \text{ Mpc}^{-1}$.

2. SAMPLE SELECTION

The COSMOS survey (Scoville et al. 2007) provides a multi-wavelength characterization of over 1.5 million galaxies at redshift extending out to 5 in 2 deg^2 of the sky. The *Chandra* X-ray coverage (C-COSMOS Elvis et al. 2009) over 0.9 deg^2 , gives us the means to study the X-ray emission of ETGs, extending local studies to higher redshifts, and explore the redshift evolution of hot halos with large samples of galaxies.

Our ETG sample is selected from the most recent version of the COSMOS photometric catalog by Ilbert et al. (2009). The spectral energy distribution (SED) identification performed by Ilbert et al. (2009) makes use of seven elliptical galaxy templates with ages

from 2–13 Gyr (Polletta et al. 2007). The SED templates were generated with the stellar population synthesis package developed by Bruzual & Charlot (2003), assuming an initial mass function from Chabrier (2003) and an exponentially declining star formation history. We also collected additional galaxy properties (stellar mass, age, and star formation rate) from Ilbert et al. (2010), and we made use of the most recent near-IR photometry from the Ultra Deep Survey with the VISTA telescope (Ultra-VISTA McCracken et al. 2012).⁴

We selected galaxies classified as E or S0 that have a reliable photometric redshift (Ilbert et al. 2009). In addition we selected only sources with Ultra-VISTA detection in both the J and K bands, since these are needed to evaluate the rest frame L_K (see below). This narrows our sample to 10,808 (the COSMOS ETG sample considered in C14). We then selected only the 6436 ETGs falling in the C-COSMOS field, and then excluded the 48 X-ray detected ETGs in common with the C-COSMOS identification catalog (Civano et al. 2012). This leads us to our final sample of 6388 C-COSMOS ETGs—not detected in X-rays—which constitutes the starting point of the stacking analysis described in this paper. Note that we selected sources with photometric redshift estimates in the catalog by Ilbert et al. (2009), while C14 selected their sources to have a spectroscopic or photometric redshift estimate in the C-COSMOS identification catalog, so the sample of ETGs selected by the latter authors (~6600 sources) is not fully contained in our sample.

Following C14 we evaluated the K-band luminosity of our sources from the Ultra-VISTA K-band aperture magnitude of the COSMOS photometric catalog. To calculate the rest-frame K-band luminosities, we assumed a power-law spectrum (as appropriate over this small frequency range) $f_\nu \propto \nu^{-\alpha}$ with $\alpha = (J - K)/2.5 \log(\nu_J/\nu_K)$ (where J and K are the AB magnitudes from the COSMOS photometric catalog and ν_J and ν_K are the corresponding frequencies), and express the rest-frame luminosities in solar luminosities as $L_K = 10^{-(K+\text{ext}-5.19)/2.5} \times (1+z)^{\alpha-1} \times (D_L/10)^2$, where z is the photometric redshift from the COSMOS catalog, D_L is the luminosity distance expressed in parsecs, and ext is the aperture correction parameter computed from the FWHM measured for all the COSMOS extended sources in the *Hubble Space Telescope* (HST)-ACS data.

We compared the distributions of the physical parameters of the 6388 C-COSMOS ETGs with the entire 10,808 COSMOS ETG sample finding no significant differences, demonstrating as expected that the sample of ETGs not detected in X-rays is representative of COSMOS ETGs overall. Note that the luminosity threshold is a function of redshift because of the uniform magnitude limit of the Ultra-VISTA COSMOS survey ($K_s \sim 24$, McCracken et al. 2012). The specific star formation rate for the majority of the ETGs is in the regime where Ilbert et al. (2010) defines galaxies as quiescent, although a higher star formation rate is observed in young ETGs. The properties (luminosity, mass, star formation rate, and age) of the COSMOS ETGs are in agreement with those reported by (Moresco et al. 2013) for a sample of ETGs selected using multiple criteria (including color-color diagrams, spectra, star formation rate, and SED classification). Masses and luminosities are in agreement

⁴ Note that the stellar masses reported in the COSMOS photometric catalog, and obtained from the Bruzual & Charlot (2003) best-fit templates, do not incorporate the Ultra-VISTA K-band near-IR data. Although this is only an issue if there is any residual star formation in the ETGs, L_K , and M_* may not necessarily be completely equivalent.

Table 1
Main Features of the L_K Selected Stacking Bins

(1) Bin number	(2) Number of sources	(3) $\langle \log(L_K/L_\odot) \rangle$	(4) $\langle z \rangle$	(5) $\langle \log(\text{age yr}^{-1}) \rangle$	(6) $\langle \log(M_*/M_\odot) \rangle$	(7) S/N	(8) $\langle L_{X\text{-LMXB},0.3-8}/(10^{40} \text{ erg s}^{-1}) \rangle$	(9) HR
1	93	9.38(0.22)	0.16(0.04)	9.66(0.26)	8.93(0.27)	3.12	0.24(0.09,0.13)	0.40(0.32)
2	946	9.60(0.21)	0.62(0.34)	9.43(0.35)	8.98(0.38)	2.60	11.40(5.07,10.72)	0.24(0.38)
3	272	10.60(0.22)	0.27(0.07)	9.60(0.24)	10.07(0.33)	3.09	<0.62	>-0.45
4	190	10.65(0.19)	0.38(0.02)	9.50(0.21)	10.11(0.30)	3.00	2.11(1.45,0.26)	0.37(0.61)
5	41	10.67(0.19)	0.44(0.01)	9.43(0.19)	10.11(0.32)	3.01	12.23(5.64,0.73)	0.23(0.40)
6	43	10.56(0.19)	0.48(0.01)	9.38(0.21)	10.06(0.25)	3.24	21.48(8.62,0.67)	0.61(0.33)
7	1017	10.70(0.18)	0.80(0.19)	9.31(0.18)	9.99(0.47)	3.03	34.53(19.32,8.27)	0.40(0.39)
8	4	11.32(0.15)	0.18(0.01)	10.01(0.03)	11.01(0.17)	3.14	1.27(0.77,0.15)	0.18(0.45)
9	7	11.28(0.14)	0.21(0.01)	9.96(0.10)	10.89(0.13)	3.12	1.57(0.87,0.06)	0.05(0.52)
10	7	11.17(0.15)	0.22(0.01)	9.86(0.23)	10.78(0.15)	3.02	2.06(1.12,0.01)	<0.16
11	20	11.43(0.17)	0.24(0.02)	9.94(0.09)	11.05(0.20)	3.24	<1.64	<0.02
12	43	11.35(0.16)	0.29(0.02)	9.88(0.10)	10.93(0.21)	3.06	1.07(0.96,0.13)	-0.14(0.58)
13	59	11.31(0.19)	0.34(0.01)	9.75(0.19)	10.84(0.22)	3.21	1.71(1.60,0.13)	<0.15
14	13	11.28(0.19)	0.35(0.01)	9.73(0.16)	10.78(0.21)	3.12	7.73(3.44,0.18)	>0.06
15	13	11.39(0.16)	0.36(0.01)	9.75(0.16)	10.94(0.22)	3.04	6.53(3.61,0.01)	0.16(0.47)
16	16	11.43(0.21)	0.37(0.01)	9.72(0.22)	10.91(0.25)	3.04	6.36(3.89,0.17)	>-0.06
17	45	11.37(0.18)	0.38(0.01)	9.68(0.22)	10.88(0.23)	3.05	3.44(3.16,0.08)	<0.41
18	45	11.55(0.22)	0.39(0.01)	9.70(0.19)	11.02(0.28)	3.03	<8.34	<0.31
19	91	11.39(0.20)	0.45(0.03)	9.69(0.22)	10.89(0.24)	3.09	6.92(5.57,1.03)	0.23(0.76)
20	216	11.44(0.21)	0.59(0.06)	9.61(0.25)	10.92(0.28)	3.04	<26.36	-0.32(0.67)
21	27	11.55(0.19)	0.67(0.01)	9.57(0.23)	11.00(0.28)	3.30	45.92(19.33,0.08)	0.36(0.45)
22	161	11.46(0.21)	0.69(0.01)	9.56(0.23)	10.91(0.29)	3.06	38.05(24.83,1.38)	0.36(0.63)
23	238	11.42(0.21)	0.75(0.04)	9.45(0.19)	10.82(0.27)	3.27	45.23(30.76,5.62)	<0.25
24	59	11.45(0.23)	0.83(0.01)	9.39(0.15)	10.83(0.24)	3.78	111.59(38.68,0.45)	-0.33(0.17)
25	319	11.47(0.21)	0.86(0.02)	9.40(0.16)	10.84(0.28)	3.04	65.09(47.91,3.10)	>0.11
26	122	11.52(0.21)	0.93(0.01)	9.37(0.15)	10.84(0.30)	3.25	104.73(50.43,2.76)	-0.33(0.50)
27	565	11.48(0.20)	1.06(0.08)	9.33(0.12)	10.66(0.49)	3.04	204.40(159.37,38.54)	<0.14
28	24	11.62(0.18)	1.20(0.01)	9.40(0.06)	10.31(0.82)	3.26	1234.10(428.64,4.11)	>0.57
29	3	11.48(0.12)	1.21(0.01)	9.40(0.03)	10.85(0.14)	3.09	606.33(204.05,0.18)	0.70(0.27)
30	112	11.50(0.18)	1.25(0.04)	9.33(0.13)	10.50(0.69)	3.02	653.77(277.84,46.88)	>0.31
31	80	11.55(0.18)	1.40(0.04)	9.30(0.13)	10.56(0.64)	1.29	<1299.87	>-0.89
32	8	12.05(0.03)	0.66(0.09)	9.75(0.12)	11.59(0.05)	6.55	368.43(62.19,123.45)	-0.18(0.16)
33	27	12.10(0.09)	1.09(0.18)	9.41(0.09)	11.41(0.11)	2.31	332.98(211.58,137.06)	-0.30(0.67)

Note. Column 1: Bin number; Column 2: number of stacked sources; Column 3: average rest frame L_K in the bin (with corresponding standard deviation); Column 4: average redshift in the bin (with corresponding standard deviation); Column 5: average stellar age in the bin (with corresponding standard deviation); Column 6: average stellar mass in the bin (with corresponding standard deviation); Column 7: signal to noise ratio of the stacked signal; Column 8: average 0.3–8 X-ray luminosity after LMXB subtraction estimated from a thermal model. The first uncertainty reported in parenthesis is due to the standard deviation of counts, stellar age, and stellar mass in the bin, while the second one takes into account the additional standard deviation of redshift. Column 9: HR (with error due to standard deviation of counts, stellar age, and stellar mass in the bin). Asterisks (*) indicate unconstrained HRs.

with those of the K-selected elliptical galaxies of Jones et al. (2014), extracted from a small area of the COSMOS field.

3. ANALYSIS AND RESULTS

Below we describe the procedures followed in our stacking analysis. The results are summarized in Tables 1 and 2.

3.1. Count Extraction at ETG Positions

We used all 49 C-COSMOS observations to evaluate source and background counts for our sample of ETGs, excluding data in the ACIS-I chip gaps. We also excluded data from X-ray detected sources, removing counts within a $10''$ radius of all sources in the C-COSMOS source identification catalog (Civano et al. 2012). We replaced the excluded counts by sampling the Poisson distribution of the pixel values of nearby background regions with the DMFILTH CIAO task.⁵ When a source lay in the field of view of more than one observation, we combined the data from the different observations using the prescriptions from Puccetti et al.

(2009), excluding observations where the source was more than 10 arcmin off-axis from the aim point.

Due to the variation of the *Chandra* point spread function (PSF) radius R_{PSF} ,⁶ we used an extraction radius r_{ext} , which was determined by the source position in each observation, in order to extract an optimal fraction of X-ray photons from the diffuse halo. For sources with morphological information available in the *HST*-ACS catalog (Leauthaud et al. 2007), we adopted the source semimajor axes R as a measure of its physical extent. For sources with $R > R_{\text{PSF}}$ we adopted values of r_{ext} that were the convolution of R and R_{PSF} $\sqrt{R^2 + R_{\text{PSF}}^2}$; otherwise we adopted $r_{\text{ext}} = R_{\text{PSF}}$ as we did for sources without morphological information in the *HST*-ACS catalog. We notice, however, that sources with $R > R_{\text{PSF}}$ represent only $\sim 1\%$ of our sample, with extraction radii typically ranging between $1''$ and $7''$. The average exposure time for each source within the extraction circle, E , was then evaluated. The histogram of extracted ETG position counts is shown in Figure 1 (blue line). The small fraction of extraction

⁵ <http://cxc.harvard.edu/ciao/ahelp/dmfilth.html>

⁶ In the following we consider the *Chandra*-ACIS radius enclosing 90% of the energy.

Table 2
Same as Table 1 but for Redshift Selected Stacking Bins

(1) Bin number	(2) Number of sources	(3) $\langle \log(L_K/L_\odot) \rangle$	(4) $\langle z \rangle$	(5) $\langle \log(\text{age yr}^{-1}) \rangle$	(6) $\langle \log(M_*/M_\odot) \rangle$	(7) S/N	(8) $\langle L_{X\text{-LMB},0.3-8}/(10^{40} \text{ erg s}^{-1}) \rangle$	(9) HR
1	186	9.12(0.07)	0.29(0.10)	9.53(0.31)	8.66(0.25)	3.02	0.96(0.36,0.72)	0.54(0.33)
2	511	9.84(0.23)	0.31(0.10)	9.52(0.26)	9.28(0.34)	3.03	0.68(0.28,0.46)	-0.33(0.52)
3	129	10.42(0.06)	0.34(0.10)	9.49(0.24)	9.96(0.12)	3.07	1.88(0.85,1.20)	>0.17
4	241	10.75(0.10)	0.35(0.08)	9.56(0.22)	10.29(0.15)	3.01	1.08(0.86,0.57)	0.12(0.58)
5	97	11.01(0.04)	0.35(0.08)	9.61(0.23)	10.57(0.09)	3.11	1.77(1.33,0.94)	>-0.34
6	9	11.09(0.01)	0.32(0.08)	9.76(0.23)	10.68(0.09)	3.38	6.38(2.36,3.77)	-0.04(0.36)
7	91	11.17(0.04)	0.36(0.07)	9.70(0.22)	10.74(0.09)	3.06	2.38(1.84,1.03)	<-0.12
8	37	11.27(0.02)	0.36(0.07)	9.74(0.20)	10.85(0.08)	3.06	4.25(2.42,2.08)	0.07(0.48)
9	46	11.35(0.03)	0.35(0.07)	9.81(0.19)	10.95(0.08)	3.03	2.85(2.06,1.30)	<-0.10
10	25	11.43(0.02)	0.37(0.07)	9.80(0.20)	11.02(0.08)	3.02	6.17(3.61,2.70)	>0.42
11	20	11.48(0.01)	0.38(0.07)	9.82(0.17)	11.09(0.07)	3.10	8.66(4.38,3.50)	-0.37(0.50)
12	18	11.52(0.02)	0.36(0.07)	9.84(0.13)	11.10(0.06)	3.25	5.70(3.02,2.77)	-0.07(0.42)
13	28	11.59(0.03)	0.36(0.07)	9.86(0.10)	11.20(0.05)	3.05	3.96(2.80,1.82)	<0.50
14	13	11.69(0.02)	0.37(0.06)	9.85(0.16)	11.27(0.10)	3.13	8.90(5.04,3.12)	<-0.33
15	18	11.81(0.05)	0.38(0.06)	9.83(0.07)	11.37(0.09)	3.05	6.00(4.60,2.10)	-0.01(0.53)
16	425	9.83(0.24)	0.73(0.14)	9.38(0.37)	9.09(0.46)	3.02	43.08(15.98,20.05)	0.52(0.36)
17	1159	10.91(0.18)	0.77(0.13)	9.33(0.17)	10.26(0.38)	3.07	21.41(15.95,9.18)	0.05(0.54)
18	262	11.28(0.04)	0.79(0.13)	9.41(0.20)	10.74(0.15)	3.03	58.62(32.17,23.11)	-0.33(0.42)
19	34	11.36(0.01)	0.82(0.14)	9.45(0.21)	10.79(0.21)	3.30	131.37(47.08,52.96)	0.11(0.33)
20	111	11.40(0.02)	0.81(0.14)	9.44(0.21)	10.86(0.11)	3.04	103.10(48.81,43.24)	0.20(0.42)
21	106	11.47(0.02)	0.81(0.14)	9.45(0.21)	10.93(0.14)	3.08	115.21(55.10,47.07)	0.50(0.47)
22	274	11.61(0.05)	0.80(0.14)	9.53(0.22)	11.08(0.11)	3.07	52.12(37.39,21.70)	>-0.29
23	8	11.72(0.01)	0.77(0.10)	9.53(0.15)	11.22(0.12)	3.17	204.51(79.18,65.47)	0.18(0.37)
24	51	11.75(0.02)	0.79(0.15)	9.60(0.24)	11.24(0.10)	3.78	102.39(36.38,46.82)	<-0.59
25	86	11.84(0.04)	0.81(0.14)	9.59(0.20)	11.32(0.10)	3.03	118.48(66.52,48.44)	<0.09
26	28	11.95(0.02)	0.85(0.12)	9.57(0.19)	11.41(0.09)	3.24	149.06(60.70,33.54)	0.04(0.39)
27	15	12.04(0.02)	0.81(0.16)	9.60(0.21)	11.50(0.10)	6.03	397.82(77.91,190.80)	-0.30(0.20)
28	8	12.13(0.03)	0.86(0.16)	9.52(0.17)	11.50(0.09)	1.20	<269.42	-0.16*
29	737	11.14(0.27)	1.18(0.12)	9.30(0.20)	9.93(0.79)	3.06	402.00(188.34,102.88)	>0.20
30	127	11.68(0.06)	1.20(0.12)	9.36(0.10)	10.90(0.44)	3.25	404.13(176.27,100.36)	-0.23(0.44)
31	14	11.84(0.02)	1.25(0.15)	9.34(0.11)	11.19(0.16)	3.18	299.63(107.66,90.89)	-0.46(0.41)
32	33	12.01(0.13)	1.21(0.13)	9.38(0.05)	11.24(0.41)	2.32	557.18(342.18,144.63)	<0.36

regions with counts above ~ 5 represents off-axis sources with large extraction radii.

3.2. Background Evaluation

To evaluate the background we extracted counts from an annulus centered on the source coordinates, with inner-radius $2r_{\text{ext}}$ and outer radius $4r_{\text{ext}}$. Due to the very low signal, the background represents the largest source of uncertainty in this kind of analysis. To estimate the systematic uncertainties introduced by the evaluation of the background, we compared the results of three different methods, obtaining consistent results. First we simply evaluated the background contribution to the total source counts from the mean count value of the pixels in the whole background annulus. Second, we adopted the clipping procedure of Willott (2011, method b), which evaluates the mean count value μ —and the standard deviation σ —of all pixels within a circle of radius $4r_{\text{ext}}$ around each source position, and then sets all pixels with count values larger than $\mu + 3\sigma$ to μ . This method suppresses the noise in the background annulus, but also removes signal from the source.⁷ Lastly, we divided the background annulus into eight 45 degree sectors, and excluded all the sectors in which the mean count

⁷ For the rare cases where $\mu + 3\sigma < 1$, only pixels with two or more counts were clipped.

value was larger than $\mu + 3\sigma$, thus excluding regions of higher background without removing signal from the source. The net counts, N , obtained with all three methods are consistent within statistics, so in the following we adopted the clipping procedure of Willott (2011, method b).

To test the robustness of our results, we also extracted counts from positions on the sky offset from the ETG coordinates by random distances between $15''$ and $30''$, in both right ascension and declination. The net counts of the non-source positions are shown in Figure 1. They follow an approximately Gaussian distribution centered on zero, as expected from background fluctuations, while the ETG counts show an excess of positive signal. To test if our results were dominated by a sub-population of ETGs, we repeated the stacking procedure on sub-samples randomly drawn from the complete sample, progressively halving the sub-sample, obtaining results compatible with the full sample.

3.3. Stacking Procedure

To evaluate the count rate C for each stacked bin we stacked the observed source net counts in 0.5–7 keV range N and exposure E to obtain $C = \sum_i N_i / \sum_i E_i$. From these counts we subtracted the expected contributions from stellar sources (LMXBs and ultra-luminous X-ray sources, ULXs), and evaluated the average bin rest-frame X-ray luminosity as

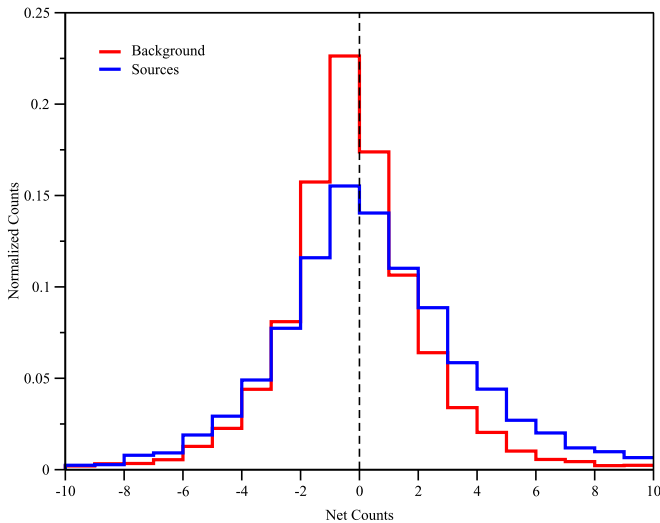


Figure 1. Distribution of net counts for randomly distributed extraction regions (red line) and for the selected sample of sources (blue line).

explained below. We corrected L_K to take into account the evolution of the stellar population (i.e., the fading effect, see C14). Note that, at a given redshift, younger galaxies have larger fading correction than older ones. To compare our results with those of KF13 and C14 we considered sources with $9 < \log(L_K) < 13$.

We constructed the stacks by binning in both L_K and z , to ensure that the binning scheme did not produce any significant bias on the results. For the L_K binning, we first divided our sample in four $\log(L_K)$ bins, 9–10, 10–11, 11–12, and 12–13. We then ordered the sources in each bin in increasing redshift, and progressively stacked them until we reached a minimum signal to noise ratio of 3; if this 3σ threshold could not be reached we stacked the signal from all the remaining sources in the bin. Examples of 0.5–7 keV images for these stacking bins are presented in Figure 2. For the z binning, we followed the same procedure, dividing the sample into three bins 0–0.5, 0.5–1, and 1–1.5, and then ordered the sources in each bin in increasing L_K .

3.4. Evaluation of Non-stellar L_X for Each Stacked Bin

To subtract the LMXB contribution from the total X-ray emission, we evaluated the average LMXB contribution to each bin using the 0.3–8 keV relation from Fragos et al. (2013b), as in C14:

$$\begin{aligned} \log(L_{\text{LMXB}}/M_*) &= 30.259 - 1.505 \times \log(\text{age}) \\ &\quad - 0.421 \times \log^2(\text{age}) + 0.425 \times \log^3 \\ &\quad \times (\text{age}) + 0.135 \times \log^4(\text{age}), \end{aligned} \quad (1)$$

where L_X is expressed in erg s^{-1} , M_* is the average stellar mass of the stacking bin expressed in solar masses and age is the average stellar age of the stacking bin expressed in Gyr.⁸ We also evaluated the contribution to X-ray luminosity from ULXs that could be present in the galaxies using the scaling relations from Calzetti et al. (2007) and Mineo et al. (2012) between the

ULX luminosity and the galaxy star formation rate. The ULX contribution is more than an order of magnitude smaller than $L_{X\text{-LMXB}}$ even for the least luminous L_K bins.

We converted the average 0.3–8 keV LMXB luminosities in each bin to count rates in the 0.5–7 keV interval using a power-law model with index $\Gamma = 1.8$ (consistent with the typical spectrum of LMXBs) and Galactic absorption $N_H = 2.6 \times 10^{20} \text{ cm}^{-2}$. For these parameters the conversion factor used from *Chandra* count rates to fluxes is $1.04 \times 10^{-11} \text{ erg cm}^{-2} \text{ s}^{-1} \text{ cts}^{-1}$.⁹ We then subtracted these count rates from the stacked signals and converted back the resulting count rates into luminosities using a model comprising Galactic N_H plus a thermal APEC component with temperature depending on the source total X-ray luminosity. We adopted $kT = 0.7, 1, \text{ and } 2 \text{ keV}$ for X-ray luminosities of $L_X < 10^{41}$, $10^{41} < L_X < 10^{42}$, and $L_X > 10^{42} \text{ erg s}^{-1}$, respectively, following BKF11 and Dai et al. (2007). Finally, we K-corrected the luminosity to the 0.3–8 keV rest-frame band. These LMXB-subtracted luminosities, which we indicate as $L_{X\text{-LMXB}}$, are expected to include the emission from the hot gaseous halos, but may also include a possible contribution from any AGN harbored within these ETGs.

Figure 3 shows the results in the $L_{X\text{-LMXB}} - L_K$ plane for both L_K and z binning (left and right panels, respectively), where on the upper axes we plot M_* as taken from COSMOS catalog. In both binning schemes the overall scatter plots are consistent, showing that we do not suffer from strong binning biases. By construction, the L_K -first binning provides information on the extreme redshift bins (both high and low), while the z -first binning covers more fully the L_K range. The bins are numbered in Figure 3, following Tables 1 and 2. We use different colors to visually divide the stacking bins into four groups: red, for bins X-ray over-luminous with respect to the local $L_{X\text{-LMXB}}$ and L_K relation (BKF11, KF13, see C14); yellow, for X-ray under-luminous bins; and gray and green for bins following the local relation with $L_{X\text{-LMXB}}$ lower and higher than $10^{41} \text{ erg s}^{-1}$, respectively.

As noted in Section 1, Equation (1) has an observed spread of a factor 2–3, which can be related to both the presence of GC LMXB in the ETGs and to the spread in age of the stellar population (Kim & Fabbiano 2004, 2010; BKF11; Lehmer et al. 2014). Given the parameter space of Figure 3, this spread will not change our conclusions.

3.5. Hardness Ratios

HRs were evaluated to characterize the ETG average spectral properties. $\text{HR} = (H - S)/(H + S)$, where S is the soft 0.5–2 keV counts and H the hard 2–7 keV counts. These HRs are those of the LMXB-subtracted emission. The contributions of these sources were evaluated and subtracted by applying the procedure in Section 3.4 to each energy band. We evaluated the errors on HRs as due to both uncertainties on counts and to uncertainties on estimate of LMXB contribution due to spread of stellar age and mass in the bins.

In Figure 4 we show the HRs for the stacking bins using the same color code as in Figure 3. We plot HR versus z in the left panel, using the L_K -first binning, which gives a better z sampling. We plot HR versus L_K in the right panel, using the z -first binning, to explore the L_K behavior. The left panel of Figure 4 shows a distinct clustering in HR- z space of bins from

⁸ These average quantities, as well as their standard deviation in each bin, are reported in Tables 1 and 2.

⁹ <http://cxc.harvard.edu/toolkit/pimms.jsp>

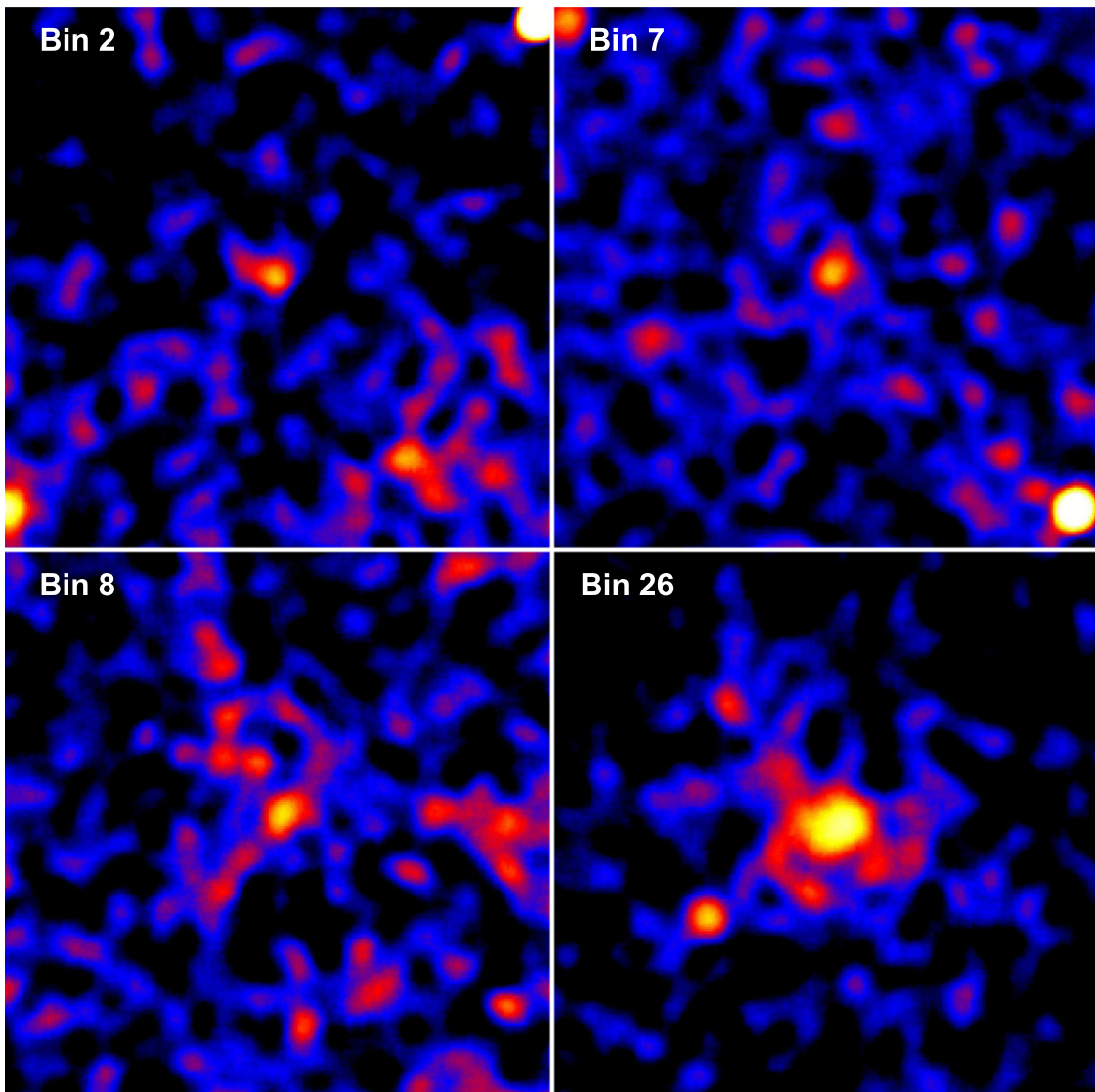


Figure 2. Examples of 0.5–7 keV images of the L_K selected stacking bins.

separate loci of the $L_{X\text{-LMXB}} - L_K$ plane, as shown by the clusters of different color points. The right panel shows that ETGs with larger stellar mass (L_K) tend to have lower HR. Given the scaling relations of ETGs (BKF11; KF13; KF15), this could just reflect a relation with total binding mass, with more massive galaxies being more efficient at retaining large hot gaseous halos.

4. DISCUSSION

Figure 5 summarizes our results in the $L_{X\text{-LMXB}} - L_K$ plane and compares them with the COSMOS ETG X-ray detections (C14) and with the near universe ETG data (BKF11, KF13). We show the local KF13 relation with a solid line, and the scatter in this relation with the two dashed lines. These lines are chosen to pass through the points for the most $L_{X,\text{gas}}$ luminous source (M87) and the most L_K luminous source (NGC1316), respectively. The COSMOS stacked-ETG results are overall consistent with the C14 COSMOS detections, but significantly increase the coverage at lower total stellar luminosities/masses. While most of the detected signals are compatible with the local KF13 relation, there are several detections that lie both to

the left and to the right of it, that is, bins that appear to be, respectively, over and under-luminous in X-rays with respect to their L_K or M_* .

In Figure 5 we also show the HRs for each stacked bin with lines with slopes proportional to HR. We find positive HRs (i.e., harder spectra) in stacked bins outside the dashed line on the left. These are the lower L_K galaxies with significant X-ray excess (the red points in Figure 4, see also C14). We also find hard HR > 0 in some points with $L_{X\text{-LMXB}} > 10^{41}$ erg s $^{-1}$ and $z > 1$ (the three top green points in Figure 4), to the left of the solid line.

Instead, lower HR ratios (i.e., softer spectra) are found in bins following the local relation (between the two dashed lines). This is especially so for those to the right of the solid line. This suggests that they have a larger than average hot gas content up to $z \sim 1$.

Figure 6 compares the HR- z scatter diagram with a set of spectral models. On the left, we show the expected HRs for thermal APEC (dashed lines; from bottom to top, $kT = 0.7, 1, 2,$ and 3 keV) and power-law models (solid lines; fixed slope $\Gamma = 2$, and increasing intrinsic absorption from bottom to top, $N_H = 0, 10^{21}, 10^{22},$ and 10^{23} cm $^{-2}$). The APEC models are the

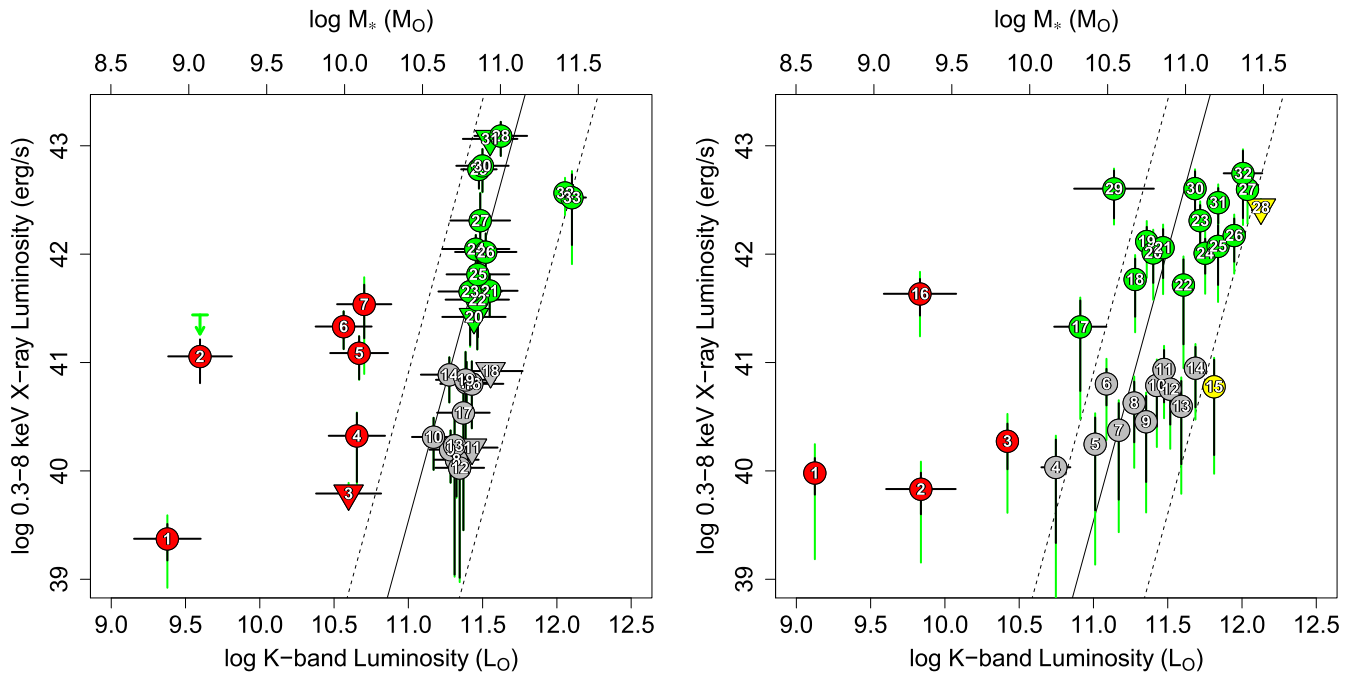


Figure 3. X-ray luminosity (after LMXBs subtraction) vs. K-band luminosity for the stacking bins selected in L_K (left panel) and redshift (right panel). The horizontal and vertical black error bars indicate the statistical uncertainties on L_K and L_{X-LMXB} , respectively, while the vertical green error bars show the uncertainty on L_{X-LMXB} due to redshift spread in each bin. The stellar mass M_* from COSMOS catalog is plotted on the top axis. The local relation by KF13 is represented with a full black line. The dashed lines are drawn to include the most $L_{X,gas}$ luminous source ETG (M87) and the most L_K luminous ETG (NGC1316) in the local sample (BKF11, KF13), respectively. Bins are labeled as in Table 1 (for the left panel) and Table 2 (for the right panel): red, X-ray over-luminous with respect to the local $L_{X,gas} - L_K$ relation; yellow, X-ray under-luminous bins; gray and green bins following the local relation with L_{X-LMXB} lower and higher than 10^{41} erg s^{-1} , respectively. Triangles pointing down represent upper limits.

expected emission of thermal gaseous emission, while the power-law models are typical AGN spectra. To illustrate cases of mixed emission from a hot gas component and a heavily obscured AGN, on the right panel of Figure 6 we plot composite models consisting of $kT = 1$ keV APEC emission with line of sight N_H plus power-law models with slope $\Gamma = 2$ and intrinsic absorption $N_H = 10^{23}$ cm $^{-2}$. From the bottom to the top the relative normalization of the two models varies, to reflect an increasing contribution of the power-law model to the total flux, ranging from $\sim 0.2\%$ to $\sim 100\%$.

The X-ray over-luminous bins (red points) have generally high HRs consistent with being dominated by AGN emission, either with “normal” AGNs with absorbing columns $\gtrsim 10^{22}$ cm $^{-2}$, or in the case of composite gas + AGN emission even highly obscured Compton thick AGNs ($N_H > 10^{24}$ cm $^{-2}$, Risaliti et al. 1999; Levenson et al. 2006; Lehmer et al. 2010).

The bins following the local relation with $L_{X-LMXB} < 10^{41}$ erg s^{-1} (gray points) show $HR \sim (-0.5) - 0.3$, lower than those of the over-luminous X-ray bins. A soft HR first suggests emission from hot gas. However, Figure 6 shows that pure APEC thermal models with solar metallicity always have $HR < -0.6$. Hence these objects have HR values inconsistent with pure gaseous emission.

These HRs can instead be explained with combinations of thermal and AGN emission. Figure 6 (right panel) shows models with varied ratios of APEC and power-law emission. In this model the observed HRs imply AGN components accounting for 15%–60% of the X-ray luminosity. Given the X-ray luminosities of this sub-sample (Figures 3 and 5), these ratios then imply AGN luminosities ranging from $\sim 5 \times 10^{39}$ erg s^{-1} to $\sim 5 \times 10^{40}$ erg s^{-1} . This range is in agreement

with the low-luminosity *Chandra* X-ray sources in the near universe sample (BKF11, Pellegrini 2005), which have luminosities ranging from $\sim 10^{38}$ erg s^{-1} to $\sim 5 \times 10^{41}$ erg s^{-1} .

The bins with $L_{X-LMXB} > 10^{41}$ erg s^{-1} (green points) have hard $HR > 0$ incompatible with a low absorption power-law model (e.g., bins 21, 22, and 25). The three highest redshift bins in this group (e.g., bins 28, 29, and 30) have even harder $HR > 0.5$ which are only compatible with absorbing columns larger than 10^{23} cm $^{-2}$. This suggests that these galaxies harbor (on average) highly obscured Compton thick AGNs that dominate their X-ray luminosity.

In summary, our stacking analysis suggests that on average AGN emission is likely to be present in ETGs. These AGNs may be faint and hidden in hot gas dominated ETGs, which are consistent with the near universe scaling relation of virialized halos (KF13, KF15, see C14). In contrast, AGN emission appears to dominate the non-stellar X-ray emission in two classes of ETGs: (1) low-stellar mass ETGs ($\log(L_K/L_{\odot}) \lesssim 10.5$), and (2) higher redshift ETGs ($z > 0.5, > 1$), in particular those over-luminous in X-rays relative to the near universe $L_{X-LMXB} - L_K$ scaling relation. The latter group has HR values suggesting highly absorbed Compton thick AGNs. We note that these AGNs were not visible in the COSMOS colors and spectra, since AGNs were excluded in our ETG sample selection process (C14).

4.1. Accretion Regimes for the AGNs

Figure 7 shows the results of the L_K -first stacking, with L_{X-LMXB} plotted against stellar mass M_* and the mass of the nuclear black hole, M_{BH} , obtained from the $M_{BH} - M_*$ relation of Kormendy & Ho (2013). Evaluating M_{BH} from the $M_{BH} - M_*$

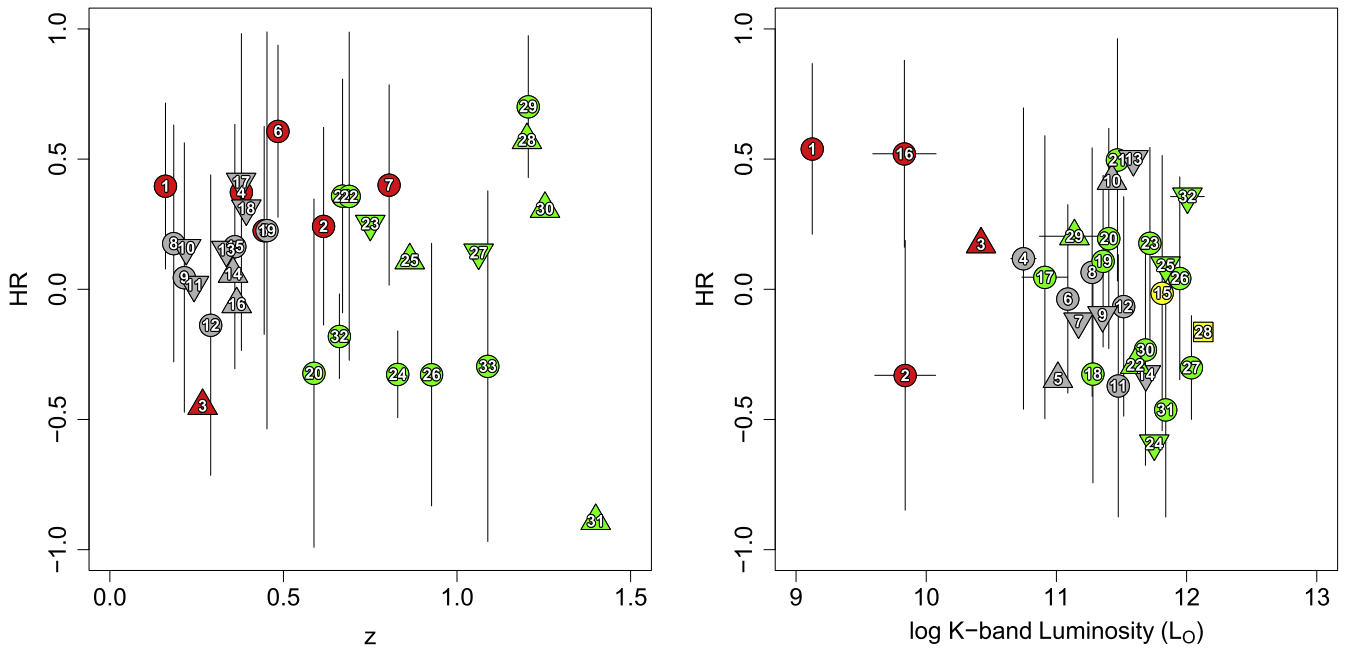


Figure 4. Left: HRs of the L_K -first stacking bins vs. redshift. Right: HRs of the z -first stacking bins vs. L_K . Triangles pointing up and down represent lower and upper limits on HR, respectively, while the box for bin 28 represents unconstrained HR.

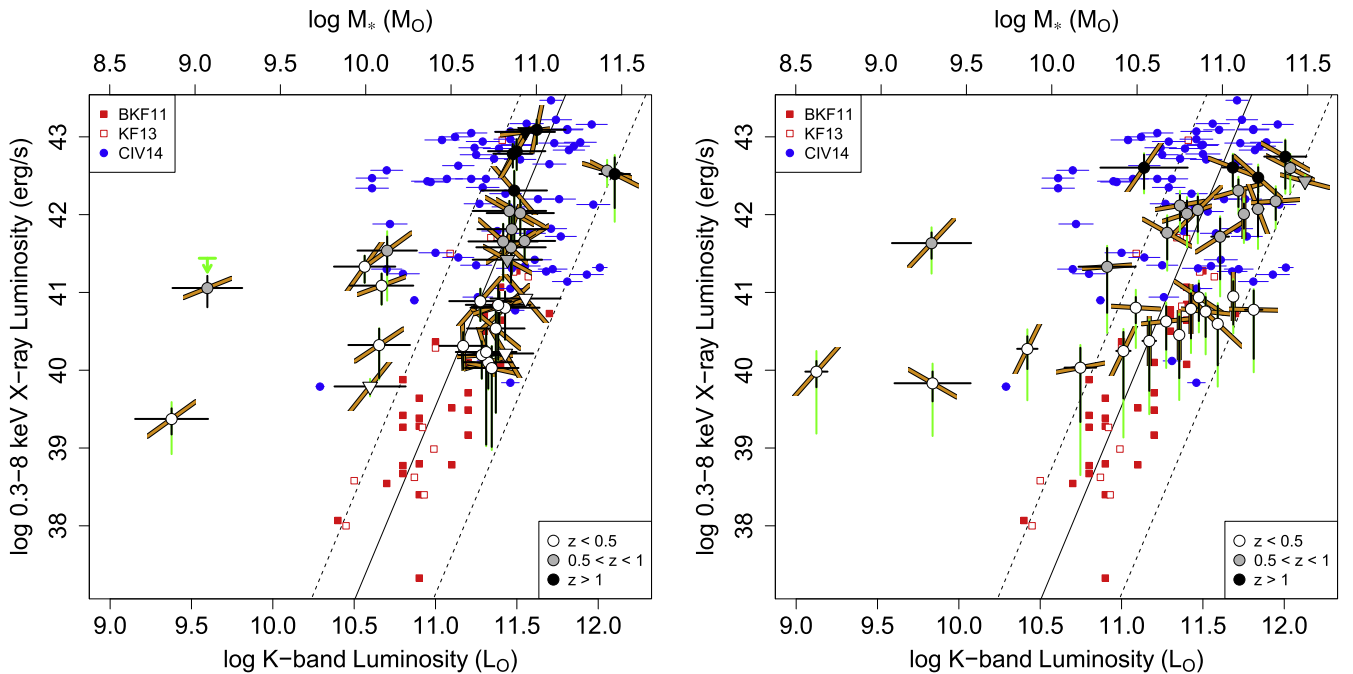


Figure 5. Same as Figure 3, but with bins labeled according to their average redshift, and HRs indicated by the slope of the orange segments. Black error bars reflect statistical uncertainties, vertical green bars show the uncertainty on L_{X-LMNB} due to redshift spread in each bin. Red boxes show the BKF11 and KF13 samples, blue circles show the CIV14 sample of C-COSMOS X-ray detected ETGs. Triangles pointing down represent upper limits.

relation of McConnell & Ma (2013) would yield black hole masses between 0.1 and 0.3 dex smaller than the former. Similarly, one could derive M_{BH} from the $M_{BH}-L_K$ relation from Graham (2007), obtaining black hole masses ~ 0.5 dex larger than the former. Uncertainties in these estimate are typically of a factor of $\sim 2-3$ (Tremaine et al. 2002; Graham 2007) and evolution to $z \sim 1-2$ may provide a systematic black hole mass increase of a similar factor (Merloni

et al. 2010). These effects will not change our conclusions in the 3 dex wide range covered by Figure 7.

On the right-hand axes we plot $L_{bol} = 10 L_{X-LMNB}$, an appropriate bolometric correction for low-luminosity AGNs that radiate at a few tens of percents of L_{Edd} (Kollmeier et al. 2006; Steinhardt & Elvis 2010). Given this nominal L_{bol} we can plot diagonal lines of constant L_{bol}/L_{Edd} . These lines range from 10^{-2} to $10^{-6} L_{bol}/L_{Edd}$.

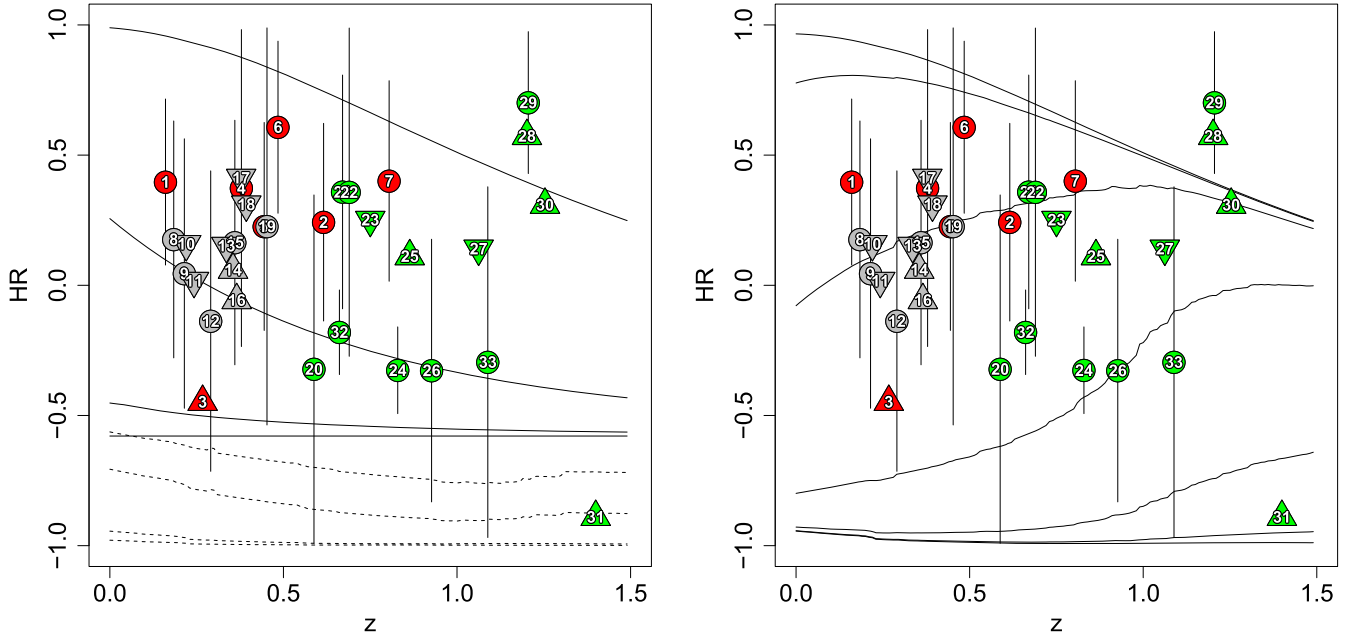


Figure 6. Left: HR- z scatter diagram of L_X -first bin. The vertical error bars indicate uncertainties on L_X -LMXB due to counts and to LMXB subtraction. Triangles pointing up and down represent lower and upper limits on HR, respectively. Squares represent unconstrained HRs. Dashed lines show HRs expected from thermal models (APEC) with increasing temperatures from bottom to top of 0.7, 1, 2, and 3 keV. The full lines represent simulated HR from power-law models with fixed slope $\Gamma = 2$ and increasing intrinsic absorption from bottom to top $0, 10^{21}, 10^{22}$, and 10^{23} cm^{-2} . Right: same as left panel, but for models comprising a power-law PL with fixed slope $\Gamma = 2$ and intrinsic absorption of 10^{23} cm^{-2} , plus a thermal model with temperature of 1 keV (APEC). The relative normalization of the two models is, from bottom to top, $10^{-3}, 10^{-2}, 10^{-1}, 1, 10, 10^2$, and 10^3 , corresponding to a contribution of the power-law component to the total flux of $\sim 0.2\%$, $\sim 2\%$, $\sim 15\%$, $\sim 62\%$, $\sim 94\%$, $\sim 99\%$, and 100% , respectively.

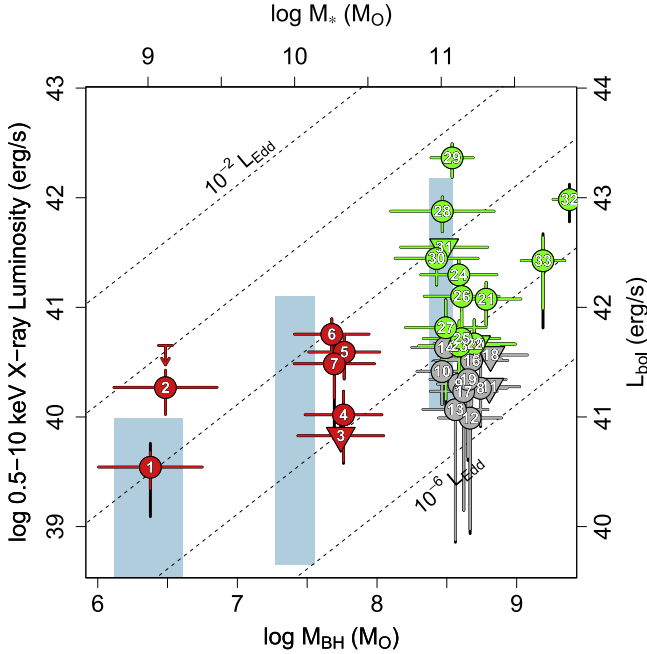


Figure 7. X-ray luminosity (after LMXBs subtraction) vs. black hole mass M_{BH} (evaluated from M_* according to the Kormendy & Ho (2013) relation) for the L_K -first stacking bins. The stellar mass M_* from the COSMOS catalog is plotted on the top axis. Lines of constant $L_{\text{bol}}/L_{\text{Edd}}$, given M_{BH} , and L_{bol} are shown as diagonals (from bottom to top $10^{-6}, 10^{-5}, 10^{-4}, 10^{-3}$, and 10^{-2}). The bins are color-labeled as in Figure 3. Light blue boxes represent the predictions of the Volonteri et al. (2011) models for $M_* = 10^9 M_\odot, 10^{10} M_\odot$, and $10^{11} M_\odot$, where the top of each box refers to radiatively efficient accretion flows and the bottom refers to RIAFs.

We see that the massive high L_X -LMXB galaxies (green points) and the low-mass X-ray over-luminous galaxies (red points) have implied Eddington ratios in the 10^{-3} to 10^{-5} range.

Radiatively inefficient accretion flows (RIAFs) are generally believed to apply to all black hole accretion below $10^{-2} L/L_{\text{Edd}}$, so we would expect all these sources to be RIAFs. If the bolometric correction for RIAFs is smaller than that considered here, as may well be the case (Narayan & Yi 1995), the L_{bol} values on the y-axis should be correspondingly lower (as the Eddington ratios on the currently plotted dashed lines).

Alternatively the true L_{bol} of the three high z bins of massive high L_X -LMXB galaxies (green points 28, 29, 30) could be greatly underestimated. The HRs of these bins also imply highly absorbed emission ($N_{\text{H}} > 10^{23} \text{ cm}^{-2}$, Figure 6). If these are then Compton thick AGNs they may have much larger intrinsic luminosities, with factors of 100 being quite plausible (e.g., Risaliti et al. 1999; Levenson et al. 2006). They would have intrinsic luminosities $L_{0.5-10 \text{ keV}} \sim 10^{45} \text{ erg s}^{-1}$ and $L_{\text{bol}}/L_{\text{Edd}}$ in the $\sim 10^{-2}$ range, so that they could lie within the normal AGN regime.

To investigate this possibility, we built SEDs of ETGs in our sample using optical-IR magnitudes reported in the COSMOS photometric catalog, since a “hidden” AGN may give rise to an IR excess with respect to an average ETG SED. We then fitted these SEDs with the same elliptical galaxy template used by Ilbert et al. (2009) without finding any significant deviation. To confirm this, we evaluated the $L_{2-10 \text{ keV}}$ luminosity of the stacking bins assuming a power-law spectrum (as appropriate for AGN spectra) and compared that with their IR luminosity. In all cases the X-ray luminosities are at least three orders of magnitude lower than the IR luminosities, even assuming absorbing columns $\sim 10^{23} \text{ cm}^{-2}$, indicating that at IR wavelengths a putative AGN component is expected to be significantly smaller than the galactic emission.

The galaxies that are consistent with the local $L_K - L_X$ -LMXB gaseous relation (gray points), with X-ray colors suggesting thermal emission plus a possible AGN component, have

smaller Eddington ratios of $\sim 10^{-5}$ to 10^{-6} (these ratios of course assume that the entire emission is due to an AGN; as shown in Figure 6, the AGN component may range from $\sim 15\%$ – 60%).

We also plot in Figure 7 the predictions from Volonteri et al. (2011) of $L_{X,AGN}$ for three values of M_* for both efficient and RIAFs (Narayan & Yi 1995). These authors' models use the stellar density profile scaling with stellar mass, and predict the accretion rate from the normal stellar mass loss due to stellar evolution, and the consequent massive black hole luminosity for various radiative efficiencies.¹⁰ The X-ray luminosity coming from accretion is computed as $L_{X,AGN}/L_{Edd} = \eta_X \eta \dot{m}$, where $\eta_X = 0.1$ is the X-ray fraction of the bolometric luminosity, and $\dot{m} = 0.1\dot{M}/M_{Edd}$ is the accretion rate in Eddington units with a 10% accretion efficiency. Radiatively efficient accretion flows have $\eta = 1$, while inefficient ones have $\eta = \dot{m}/\dot{m}_{cr}$, and for them $\dot{m} < \dot{m}_{cr} = 3 \times 10^{-2}$.

In order to compare our results with Volonteri et al. (2011) models, we converted the 0.5–7 keV LMXB-subtracted counts into 0.5–10 keV band luminosities, $L_{0.5-10\text{ keV}}$ assuming a power-law spectrum as appropriate for AGN spectra. Based on these models, inefficient accretion into the nuclei could even explain all the L_{X-LMXB} of the massive, high L_{X-LMXB} ETGs (green points), except for the most luminous ones, which are likely to be Compton thick AGNs (see above). The low-mass X-ray over-luminous ETGs (red points) are also consistent with the Volonteri et al. model. Considering that a large fraction of the X-ray emission is due to hot gas (see above), the gray points show instead a possible AGN emission even lower than predicted for radiatively inefficient accretion. In these ETGs, the L_{X-LMXB} is consistent with the local $L_{X,gas} - L_K$ relation.

This result can have the following possible explanations, which are not mutually exclusive.

1. The Volonteri et al. models assume that the whole of their estimated mass accretion rate (coming from the instantaneous mass loss of all stars, and obtained by integrating over the whole stellar density profile) indeed reaches the massive black hole, while this represents an upper limit on the mass accretion rate of the massive black hole (some gas may be outflowing, or may reach the massive black hole with a delay, or may possess angular momentum and form a disk, etc.).
2. The accreting mass, which has already entered the accretion radius, is reduced on its way to the massive black hole, due to a wind from a RIAF (Narayan & Yi 1995; Blandford & Begelman 1999); similarly, close to the nucleus, there may be a heating mechanism for the accreting gas, such as a nuclear jet, again impeding or lowering the accretion rate (e.g., Pellegrini et al. 2012; Yuan & Li 2011).
3. Accretion onto the black hole is (temporarily) not taking place, as may be the case during feedback-regulated activity cycles. Numerical simulations show that, during these cycles, AGN outbursts are followed by major degassing of the circumnuclear region, with a precipitous drop of the nuclear accretion rate; the outbursts are separated by long time intervals during which the galaxy

is replenished again by gas from the stellar mass losses, until a new nuclear outburst takes place (Ciotti et al. 2010).

4. η_X might be lower than 1 as assumed here (see also Volonteri et al. 2011), or η at low \dot{m} can decrease faster than adopted in the Volonteri et al. models, so that lower $L_{X,AGN}$ should be predicted (e.g., Yuan & Narayan 2014).

Our results extend to higher X-ray luminosities a recent analysis of ETGs in the AMUSE survey of Virgo and field galaxies with *Chandra* (Miller et al. 2015). AMUSE results indicate a significant presence of supermassive black holes (SMBHs) in low-stellar-mass galaxies. Due to the lower redshifts of the AMUSE ETGs, that survey is sensitive to X-ray luminosities ($\sim 1.3 \times 10^{38}$ erg s⁻¹) one order of magnitude fainter than our faintest bin 1 ($\sim 2.4 \times 10^{39}$ erg s⁻¹). For these dim sources the stellar wind accretion proposed by Volonteri et al. (2011) would predict higher X-ray luminosities than those observed, Miller et al. conclude that these black holes are probably powered by inefficient advection dominated accretion flows or, alternatively, by an outflow/jet component. We found that low-luminosity, X-ray “over-luminous” ETGs can be adequately described by the RIAF fueled by stellar winds as proposed by Volonteri et al. (2011). Instead, ETGs with $L_{X-LMXB} > 10^{42}$ erg s⁻¹ may host Compton thick AGNs. Similarly, when comparing our results with those of Lehmer et al. (2007) and Danielson et al. (2012) on *Chandra* Deep Fields, we extend to higher X-ray luminosities and to lower optical luminosities (that is, lower stellar masses), finding sources that significantly exceed the expected emission from hot-gas dominated ETGs, with $\log(L_{0.5-2\text{ keV}}/L_B)/(\text{erg s}^{-1}/L_\odot) > 30$ (see Figure 7 in Danielson et al. 2012).

We also note that, as reported by Comastri et al. (2015), the revision of black hole scaling relations by Kormendy & Ho (2013) indicates that the local mass density in black holes should be five times higher than previous estimates. These authors advance the possibility that a sizeable population of highly obscured AGNs with a covering fraction of obscuring material $\sim 4\pi$ would explain the revised upward value of the SMBH local mass density without exceeding the limits imposed by the X-ray and IR background. An example of these obscured AGNs could be that observed in the ETG ESO565-G019 with *Suzaku* and *Swift*/BAT (Gandhi et al. 2013).

Finally, we note that the hard X-ray slopes of the more luminous ETG bins could be due to contamination from X-ray jets. However, the combined 1.4 GHz VLA COSMOS Large and Deep Project catalogs (Schinnerer et al. 2010) offer radio counterparts only to $\sim 2\%$ of our sample of ETGs. The presence of radio emitters among non-X-ray detected ETGs will be addressed after the release of the JVLA-COSMOS Project data.

5. SUMMARY AND CONCLUSIONS

We have followed up our previous work (C14) investigating the X-ray/K-band properties of the 69 ETGs detected in the *Chandra* COSMOS survey (Elvis et al. 2009), with a luminosity and HR stacking analysis of the *Chandra* data for the sample of 6388 ETGs not detected in X-rays. The stacking analysis allows the investigation of the average features of individual X-ray undetected ETGs. Our ETG sample was selected as representative of normal galaxies, with no evidence of AGN emission in their spectra and multi-band photometry

¹⁰ We note that in Volonteri et al. (2011) the models assume a stellar age of 12 Gyr for ETGs. We corrected for the average age $10^{9.5}$ Gyr of C-COSMOS ETGs, which yields slightly smaller emitted X-ray luminosities (see Equation (9) in Volonteri et al. 2011).

(C14, Section 2). Our purpose was to investigate the properties of the X-ray emission from hot gas and from possible “hidden” AGN components that may be revealed by their X-ray emission. To this purpose, the expected contribution of LMXBs was subtracted from the X-ray luminosity of each stacked bin, using established scaling relations with the K-band luminosity (BKF11). All luminosities were corrected to the local rest frame; X-ray HRs were based on the observed counts (after subtraction of the LMXB contribution), and were compared to emission models for the appropriate average bin redshift.

This analysis has led to the following conclusions:

1. On average AGN emission may be present in all ETGs.
2. AGNs may be faint and hidden in hot gas dominated ETGs, which are consistent with the local universe scaling relation of virialized halos (KF13, KF15, see C14).
3. AGN emission appears to dominate the non-stellar X-ray emission in low-stellar mass ETGs ($\log(L_K) \lesssim 10.5$ in solar units), which show marked X-ray luminosity excesses relative to their K-band luminosity (a proxy of stellar mass) when compared with the local ETG $L_{X,\text{Gas}}L_K$ relation of the local universe (BKF11). This result confirms the conclusions of C14 and extends them to lower stellar mass galaxies.
4. AGN emission is also prominent in higher redshift ETGs ($z > 0.5$, > 1), in particular those with X-ray luminosity $\gtrsim 10^{42}$ erg s $^{-1}$. The latter group have HR values suggesting highly absorbed Compton thick AGNs. We note that these AGNs were not visible in the COSMOS colors and spectra, since AGNs were excluded by our ETG sample (C14).
5. Given the nuclear BH mass predicted by the $M_{\text{BH}} - L_K$ relation (Kormendy & Ho 2013), the hidden AGNs in the X-ray over-luminous low-stellar-mass ETGs are consistent with the presence of radiatively inefficient accretion fueled by stellar outgassing (Volonteri et al. 2011). The highly absorbed higher $L_{X\text{-LMXB}}$ AGNs hidden in massive, higher z ETGs instead suggest efficient accretion in highly obscured nuclei.

This work was partially supported by NASA contract NAS8-03060 (CXC), and NASA *Chandra* grant G01-12110X. S.P. acknowledges financial support from MIUR grant PRIN 2010-2011, project “The Chemical and Dynamical Evolution of the Milky Way and Local Group Galaxies,” prot. 2010LY5N2T. F.C. acknowledges financial support by the NASA contract 11-ADAP11-0218. A.P. thanks Andy Goulding for useful discussion and suggestions. M.E. and G.F. thank the Aspen Center for Physics and the NSF Grant #1066293 for hospitality during the completion of this paper. This research has made use of software provided by the *Chandra* X-ray Center (CXC) in the application packages CIAO, ChIPS, and Sherpa. This research is based on observations collected at the European Organisation for Astronomical Research in the Southern Hemisphere, Chile, program 179.A-2005 (Ultra-VISTA survey).

REFERENCES

Blandford, R. D., & Begelman, M. C. 1999, *MNRAS*, 303, L1
 Boroson, B., Kim, D.-W., & Fabbiano, G. 2011, *ApJ*, 729, 12 (BKF11)

Bruzual, G., & Charlot, S. 2003, *MNRAS*, 344, 1000
 Calzetti, D., Kennicutt, R. C., Engelbracht, C. W., et al. 2007, *ApJ*, 666, 870
 Canizares, C. R., Fabbiano, G., & Trinchieri, G. 1987, *ApJ*, 312, 503
 Chabrier, G. 2003, *PASP*, 115, 763
 Ciotti, L., D’Ercole, A., Pellegrini, S., & Renzini, A. 1991, *ApJ*, 376, 380
 Ciotti, L., & Ostriker, J. P. 2007, *ApJ*, 665, 1038
 Ciotti, L., Ostriker, J. P., & Proga, D. 2010, *ApJ*, 717, 708
 Civano, F., Elvis, M., Brusa, M., et al. 2012, *ApJS*, 201, 30
 Civano, F., Fabbiano, G., Pellegrini, S., et al. 2014, *ApJ*, 790, 16 (C14)
 Comastri, A., Gilli, R., Marconi, A., Risaliti, G., & Salvati, M. 2015, *A&A*, 574, L10
 Cox, T. J., Di Matteo, T., Hernquist, L., et al. 2006, *ApJ*, 643, 692
 Dai, X., Kochanek, C. S., & Morgan, N. D. 2007, *ApJ*, 658, 917
 Danielson, A. L. R., Lehmer, B. D., Alexander, D. M., et al. 2012, *MNRAS*, 422, 494
 David, L. P., Forman, W., & Jones, C. 1991, *ApJ*, 369, 121
 Elvis, M., Civano, F., Vignali, C., et al. 2009, *ApJS*, 184, 158
 Fabbiano, G. 1989, *ARA&A*, 27, 87
 Fabbiano, G. 2006, *ARA&A*, 44, 323
 Forman, W., Schwarz, J., Jones, C., Liller, W., & Fabian, A. C. 1979, *ApJL*, 234, L27
 Fragos, T., Lehmer, B., Naoz, S., Zezas, A., & Basu-Zych, A. 2013, *ApJL*, 776, L31
 Fragos, T., Lehmer, B., Tremmel, M., et al. 2013, *ApJ*, 764, 41
 Gandhi, P., Terashima, Y., Yamada, S., et al. 2013, *ApJ*, 773, 51
 Garmire, G. P., Bautz, M. W., Ford, P. G., Nousek, J. A., & Ricker, G. R., Jr. 2003, *Proc. SPIE*, 4851, 28
 Gilfanov, M. 2004, *MNRAS*, 349, 146
 Graham, A. W. 2007, *MNRAS*, 379, 711
 Ilbert, O., Capak, P., Salvato, M., et al. 2009, *ApJ*, 690, 1236
 Ilbert, O., Salvato, M., Le Floch, E., et al. 2010, *ApJ*, 709, 644
 Jones, T. M., Kriek, M., van Dokkum, P. G., et al. 2014, *ApJ*, 783, 25
 Kim, D.-W., & Fabbiano, G. 2004, *ApJ*, 611, 846
 Kim, D.-W., & Fabbiano, G. 2010, *ApJ*, 721, 1523
 Kim, D.-W., & Fabbiano, G. 2013, *ApJ*, 776, 116 (KF13)
 Kim, D.-W., & Fabbiano, G. 2015, *ApJ*, 812, 127
 Kim, D.-W., Fabbiano, G., Brassington, N. J., et al. 2009, *ApJ*, 703, 829
 Kollmeier, J. A., Onken, C. A., Kochanek, C. S., et al. 2006, *ApJ*, 648, 128
 Kormendy, J., & Ho, L. C. 2013, *ARA&A*, 51, 511
 Kundu, A., Maccarone, T. J., & Zepf, S. E. 2002, *ApJL*, 574, L5
 Leauthaud, A., Massey, R., Kneib, J.-P., et al. 2007, *ApJS*, 172, 219
 Lehmer, B. D., Alexander, D. M., Bauer, F. E., et al. 2010, *ApJ*, 724, 559
 Lehmer, B. D., Berkeley, M., Zezas, A., et al. 2014, *ApJ*, 789, 52
 Lehmer, B. D., Brandt, W. N., Alexander, D. M., et al. 2007, *ApJ*, 657, 681
 Levenson, N. A., Heckman, T. M., Krolik, J. H., Weaver, K. A., & Życki, P. T. 2006, *ApJ*, 648, 111
 Mathews, W. G., & Brighenti, F. 2003, *ARA&A*, 41, 191
 McConnell, N. J., & Ma, C.-P. 2013, *ApJ*, 764, 184
 McCracken, H. J., Milvang-Jensen, B., Dunlop, J., et al. 2012, *A&A*, 544, A156
 Merloni, A., Bongiorno, A., Bolzonella, M., et al. 2010, *ApJ*, 708, 137
 Miller, B. P., Gallo, E., Greene, J. E., et al. 2015, *ApJ*, 799, 98
 Mineo, S., Gilfanov, M., & Sunyaev, R. 2012, *MNRAS*, 419, 2095
 Moresco, M., Pozzetti, L., Cimatti, A., et al. 2013, *A&A*, 558, A61
 Narayan, R., & Yi, I. 1995, *ApJ*, 452, 710
 Pellegrini, S. 2005, *ApJ*, 624, 155
 Pellegrini, S., Wang, J., Fabbiano, G., et al. 2012, *ApJ*, 758, 94
 Polletta, M., Tajer, M., Maraschi, L., et al. 2007, *ApJ*, 663, 81
 Puccetti, S., Vignali, C., Cappelluti, N., et al. 2009, *ApJS*, 185, 586
 Risaliti, G., Maiolino, R., & Salvati, M. 1999, *ApJ*, 522, 157
 Sarazin, C. L., Irwin, J. A., & Bregman, J. N. 2000, *ApJL*, 544, L101
 Schinnerer, E., Sargent, M. T., Bondi, M., et al. 2010, *ApJS*, 188, 384
 Scoville, N., Abraham, R. G., Aussel, H., et al. 2007, *ApJS*, 172, 38
 Steinhardt, C. L., & Elvis, M. 2010, *MNRAS*, 402, 2637
 Tremaine, S., Gebhardt, K., Bender, R., et al. 2002, *ApJ*, 574, 740
 Trinchieri, G., & Fabbiano, G. 1985, *ApJ*, 296, 447
 Tzanavaris, P., & Georgantopoulos, I. 2008, *A&A*, 480, 663
 Volonteri, M., Dotti, M., Campbell, D., & Mateo, M. 2011, *ApJ*, 730, 145
 White, R. E., III, & Sarazin, C. L. 1991, *ApJ*, 367, 476
 Willott, C. J. 2011, *ApJL*, 742, L8
 Yuan, F., & Li, M. 2011, *ApJ*, 737, 23
 Yuan, F., & Narayan, R. 2014, *ARA&A*, 52, 529